N-terminal domain of αB-crystallin provides a conformational switch for multimerization and structural heterogeneity

Stefan Jehle[a], Breanna S. Vollmar[a], Benjamin Bardiaux[b], Katja K. Dove[a], Ponni Rajagopal[a], Tamir Gonen[a,c,1], Hartmut Oschkinat[b,d,1], and Rachel E. Klevit[a,1]

[a]Department of Biochemistry, University of Washington, Seattle, WA 98195; [c]Howard Hughes Medical Institute, University of Washington, Seattle, WA 98195; [b]Leibnizinstitut für Molekulare Pharmakologie, Robert-Rössle-Strasse 10, 13125 Berlin, Germany; and [d]Freie Universität Berlin, Takustrasse 3, 14195 Berlin, Germany

Edited by Arthur L. Horwich, Yale University School of Medicine, New Haven, CT, and approved February 18, 2011 (received for review September 30, 2010)

The small heat shock protein (sHSP) αB-crystallin (αB) plays a key role in the cellular protection system against stress. For decades, high-resolution structural studies on heterogeneous sHSPs have been confounded by the polydisperse nature of αB oligomers. We present an atomic-level model of full-length αB as a symmetric 24-subunit multimer based on solid-state NMR, small-angle X-ray scattering (SAXS), and EM data. The model builds on our recently reported structure of the homodimeric α-crystallin domain (ACD) and C-terminal IXI motif in the context of the multimer. A hierarchy of interactions contributes to build multimers of varying sizes: Interactions between two ACDs define a dimer, three dimers connected by their C-terminal regions define a hexameric unit, and variable interactions involving the N-terminal region define higher-order multimers. Within a multimer, N-terminal regions exist in multiple environments, contributing to the heterogeneity observed by NMR. Analysis of SAXS data allows determination of a heterogeneity parameter for this type of system. A mechanism of multimerization into higher-order asymmetric oligomers via the addition of up to six dimeric units to a 24-mer is proposed. The proposed asymmetric multimers explain the homogeneous appearance of αB in negative-stain EM images and the known dynamic exchange of αB subunits. The model of αB provides a structural basis for understanding known disease-associated missense mutations and makes predictions concerning substrate binding and the reported fibrilogenesis of αB.

Small heat shock proteins (sHSPs) help to maintain protein homeostasis by interacting with partly folded substrates to prevent cell damage (1–3). The ATP-independent chaperone αB-crystallin (αB, 20 kDa, 175 residues) is an archetypal example (4). Discovered as a highly abundant protein in the eye lens that plays a critical role in maintenance of lens transparency, the known biological roles of αB continue to expand. The protein is expressed in many tissue types, notably muscle and brain, in a stress-inducible manner, where it presumably serves as a chaperone for misfolded cellular proteins. Consistent with such a role, αB is implicated in a growing number of diseases that includes cardiac myopathies and neurodegenerative diseases such as Alexander disease and Alzheimer's disease (5–7). Furthermore, αB has been shown to play a protective role and can reverse symptoms of multiple sclerosis (8). Thus, a full structural description of αB is an important step toward understanding its mode(s) of action. Past models of αB have been based on biochemical data (9); however, recent advances in structural biology of sHSPs (9–11) allow for a more detailed understanding of the assembly of αB multimers.

As for all sHSPs, αB is organized in three domains (Fig. 1*A*): (*i*) an N-terminal domain of approximately 60 residues, (*ii*) a central α-crystallin domain (ACD) of about 90 residues involved in dimerization (Fig. S1*A*), and (*iii*) a C-terminal domain of 25 residues containing the IXI motif, usually comprised of two Ile residues separated by an intervening residue, that is highly conserved in sHSPs. Recent studies using solid-state NMR and X-ray crystallography have yielded atomic-level structures of ACDs from polydisperse mammalian sHSPs, which have been refractory to structure determination (10–12). We reported a structure determined from solid-state NMR measurements on full-length αB in which a highly curved homodimer comprised of two ACDs forms the basic building block of multimers (10). A recent EM structure of negatively stained αB showed a tetrahedrally symmetric oligomer representing the shape of a 24-mer (13). This arrangement could be recapitulated from the curved dimer structure solved by solid-state NMR and an approximate oligomer shape from small-angle X-ray scattering (SAXS) (10). αB is a highly dynamic species in which multimers ranging from 24 to 32 subunits coexist and exchange rapidly (14), and although the aforementioned structures represent a significant advance in αB structural biology, they do not address the hallmark heterogeneity of αB and other sHSPs. Moreover, structural aspects of the N-terminal domain of αB remain poorly understood.

Here we present a model of the N-terminal region (residues 1–65) based on solid-state NMR restraints and similar fragments from proteins in the Protein Data Bank (PDB). Our analysis identifies two β-strands that exist in multiple structural environments. We present a model for full-length αB as a tetrahedrally symmetrical 24-mer based on the published EM map of αB (13). Next we use SAXS to measure αB heterogeneity in solution and together with additional EM analysis we propose a model in which additional dimeric units can fill existing openings in a 24-mer to create higher-order multimers that look alike in negatively stained preparations in electron microscopy.

Results

The N and C Termini of αB Are Highly Flexible. The domain organization of αB is shown schematically in Fig. 1*A*. Solution-state NMR measurements on αB oligomers have revealed that the first 5 N-terminal and the last 10–12 C-terminal residues are flexible (15, 16). The methyl resonance region of a 2D ^{1}H-^{13}C INEPT MAS solid-state NMR spectrum of an αB preparation precipitated with PEG 8000 contains a number of intense, sharp peaks that arise from flexible residues (Fig. 1*B*). Based on chemical shift similarity with the solution-state NMR spectra, we assign the resonances to Met1 and the methyl-containing side chains at the extreme C terminus of αB (Ala168, Val169, Thr170, Ala171,

Author contributions: S.J., P.R., T.G., H.O., and R.E.K. designed research; S.J., B.V., B.B., and K.K.D. performed research; S.J., B.V., B.B., K.K.D., T.G., H.O., and R.E.K. analyzed data; and S.J., B.V., K.K.D., P.R., T.G., H.O., and R.E.K. wrote the paper.

The authors declare no conflict of interest.

This article is a PNAS Direct Submission.

[1]To whom correspondence may be addressed. E-mail: tgonen@uw.edu, oschkinat@fmp-berlin.de, or klevit@uw.edu.

This article contains supporting information online at www.pnas.org/lookup/suppl/doi:10.1073/pnas.1014656108/-/DCSupplemental.

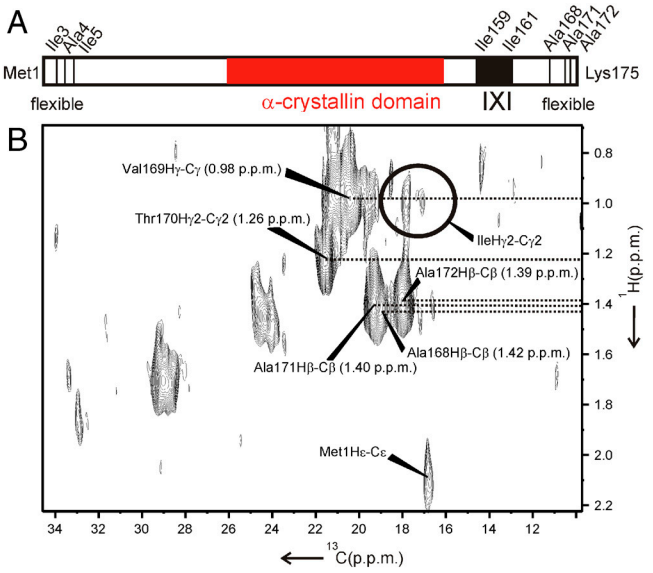

Fig. 1. (*A*) Domain architecture of αB: an N-terminal domain essential for oligomerization, an α-crystallin domain involved in dimerization, and a C-terminal domain containing the conserved IXI motif. (*B*) 2D ^{1}H-^{13}C INEPT MAS solid-state NMR spectrum show flexible residues in N and C termini; assignments from Carver et al. (15) are indicated with dotted lines.

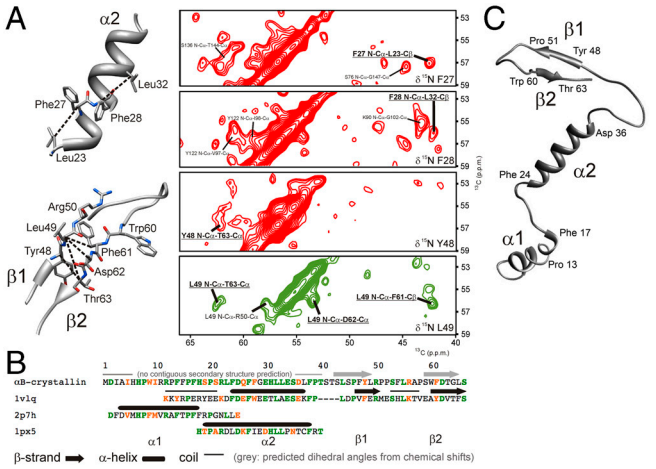

Fig. 2. (*A*) Contour plots from 3D NCACX spectra measured by solid-state NMR recorded using 500-ms spin-diffusion mixing. Distance restraints support secondary structure for the N terminus. Data were collected from αB expressed with either 1,3-[^{13}C]-glycerol (green contours) or 2-[^{13}C]-glycerol (red contours). Correlations that define the relevant distant restraints are underlined. (*B*) Sequence alignment of the N terminus of αB with similar protein fragments. The residue numbering is for αB. (*C*) Model of the N-terminal domain of αB residues 1–65 based on solid-state NMR restraints, dihedral angles from chemical shifts, and similarity to 1vlq (β1, β2, α2) and 2p7h (α1). Residue numbers indicate the first and last residues of secondary structure. Pro13 and Phe17 (indicated) flank the region where NMR restraints are observed.

and Ala172). This region of the INEPT spectrum also contains distinct but weaker signals in positions consistent with isoleucines, likely from the extreme N-terminal region (Ile3, Ile5, and potentially Ile10). These observations indicate that the highly flexible termini observed in solution are also flexible in αB preparations precipitated with PEG 8000.

Secondary Structure Within the N-Terminal Domain of αB. Compared to the well-defined ACD, most residues in the N-terminal domain have low signal intensity and chemical shift dispersion in solid-state NMR spectra. Multiple chemical shift sets for individual residues complicated the assignment and detection of structural restraints. Nevertheless, we were able to assign resonances for a majority of residues in the N-terminal domain (Biological Magnetic Resonance Bank entry 16391) (17, 18). Backbone resonance chemical shifts analyzed using TALOS (19) predict β-strand structure for residues Leu44-Tyr48 and Ser59-Thr63. Distance restraints observed between the $^{13}C\alpha$ resonances of Tyr48 and Thr63 and between the $^{13}C\alpha$ resonance of Leu49 and the $^{13}C\alpha$ resonance of Asp62 and Thr63 and $^{13}C\beta$ resonance of Phe61 further corroborate the prediction and indicate an antiparallel orientation between the two strands (Fig. 2*A* and Table S1). Although the chemical shift analysis did not yield a high confidence prediction of other regular secondary structure in the N-terminal region, eight distance restraints observed in 3D NCACX and NCOCX spectra indicate that residues 14–17 and 27–32 adopt helical conformations, as typical (i, $i+3$) and (i, $i+4$) correlations could be identified for these residues (illustrated in Fig. 2*A* and summarized in Table S1).

Modeling the N-Terminal Domain of αB. To augment the sparse experimental restraints observed for the N-terminal domain, we performed a sequence similarity search for αB residues 1–65 against proteins in the PDB to detect fragments with known structures. Three significant matches were identified (Fig. 2*B* and Table S2). The longest match was for αB residues 12–66 with residues 12–62 of acetyl xylan esterase from *Thermotoga maritima* (PDB 1vlq, 47% similarity, Table S2). Notably, the esterase structure contains β-strands that align with the two predicted strands in αB. In the esterase, the strands form a two-stranded antiparallel sheet connected by a long loop. Esterase residues 23–37 form an α-helix and align with αB residues 23–37, which give helical distance restraints. Two shorter αB sequences gave significant similarity scores: with residues 5–27 of 2′-specific/double-stranded RNA-activated interferon-induced antiviral protein 2′-5′-oligoadenylate synthetase (PDB 1px5, 65% similarity, Table S2) and with residues 25–48 of methyltransferase-fold protein from *Erwinia carotovora atroseptica* (PDB 2p7h, Table S2). Helical secondary structure is predicted for αB residues 19–38 based on the alignment with a fragment of the synthetase, corroborating the prediction based on the esterase. αB residues 2–25 have 54% similarity with N-terminal residues of the methyltransferase fold protein. Taken together, the solid-state NMR observations and sequence alignments are consistent with the N-terminal domain containing two helical segments and an antiparallel β1-loop-β2 structure comprised of residues 44–65.

The heterogeneity of NMR signals observed for the N-terminal region indicates that the structures described above do not all exist simultaneously in the same environment in all copies of αB subunits in all multimers. For simplicity, a model of the N-terminal region that includes all these structural features was generated by fusing the relevant fragments of the esterase and the methyltransferase-fold protein, as shown in Fig. 2*C*. A fragment (residues 1–20) that contains helix α1 and a fragment containing α2, β1, and β2 (residues 21–65) were modeled based on 2p7h and 1vlq (Fig. S2), respectively. The resulting fragments were connected and energy minimized using the solid-state NMR restraints with Discovery Studio (Accelrys).

Building a Multimer Model. Our previous NMR studies defined the ACD homodimer as the basic building block of αB oligomers. Three dimers form a triangular array on the surface of a multimer, each connected via its IXI motif bound in the groove between the β4 and β8 strands of a neighboring dimer (Fig. 3*A* and Fig. S1 *B* and *C*) (10). A similar arrangement is observed in the octahedrally symmetrical oligomer of sHSP 16.5 from *Methanococcus janashii* (Fig. S1*D*) (20), suggesting that a triangular arrangement of dimers is a conserved structural motif among sHSPs.

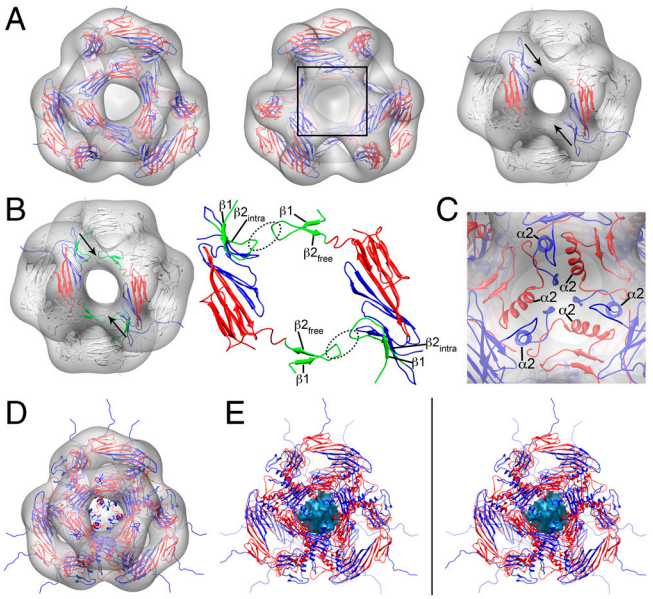

Fig. 3. Model of αB 24-mer. (*A*) Triangular arrangement of three ACD dimers (PDB 2klr, residues 69–151) connected via the IXI motif of a neighboring dimer (residues 152–165) fit into EM density (EMD-1776) (13) (see also Fig. S8). (*Left* and *Center*) A threefold axis is shown viewed from the near and far side, respectively; (*Right*) view onto a twofold axis. Unfilled density is indicated by the square (*Center*) and arrows (*Right*). (*B*) View onto a twofold axis. (*Left*) N-terminal residues 45–68 (β1-loop-$\beta 2_{free}$) fitted into unfilled EM density, marked by arrows; (*Right*) same view, with EM density removed to illustrate different environments of β1/β2 loops. The tips of two loops (indicated by dashed circles) are close to each other and result in cross-linking of single cysteine mutants. (*C*) Enlargement of the area denoted by the square in *A, Center*, showing N-terminal residues 10–39 placed into the threefold axes of the 24-mer (see text for details). (*D*) Flexible residues 166–175 are on the surface for half the subunits and point to the inside of the 24-mer in the other half. Residues 1–10 reside on the inside. (*E*) Stereoview of 24-mer illustrating the small inner hollow (central blue sphere) surrounded by flexible residues from the N and C termini.

Four copies of triangular hexamers comprised of the ACD and the C-terminal region were fitted into the published EM density of αB (EMDataBank entry EMD-1776) (13), which exhibits tetrahedral symmetry (Fig. 3*A*). This arrangement results in four threefold axes and three twofold axes (Fig. 3*A*). Views onto the threefold and twofold axes each revealed density in the EM map that was not yet accounted for that likely originates from N-terminal domain residues (boxed region and indicated with arrows, respectively, in Fig. 3*A*). In the esterase structure (1vlq), the loop connecting β1 and β2 contacts another subunit's loop, forming a ring-like assembly within the multimeric structure (Fig. S2). αB constructs lacking the N-terminal domain (e.g., αB 69–175) fail to form large multimers, consistent with involvement of N-terminal residues in multimer formation (21, 22). We therefore positioned the β1-loop-β2 model comprised of αB residues Ser45-Leu65 in an orientation analogous to the esterase into empty EM density observed in the twofold axis (Fig. 3*B*).

Placement of the β1/β2 loops into the 24-mer as described above results in two environments for this structural element (shown schematically in Fig. S3*A*). β1/β2 of one subunit within a homodimer contacts the β3 strand of its own ACD while the other β1/β2 crosses a twofold axis; its β2 does not contact a β3. We distinguish these as $\beta 2_{intra}$ and $\beta 2_{free}$, respectively (Fig. 3*B*). A third environment for β1/β2, called $\beta 2_{inter}$, arises in multimers with greater than 24 subunits (described below). We refer to β2 as originally defined from X-ray structures (11, 12). However, our NMR restraints and the sequence similarities with other known structures suggest that $\beta 2_{intra}$ is longer (i.e., spanning residues 60–69), whereas $\beta 2_{free}$ and $\beta 2_{inter}$ are shorter (spanning residues 60–63), with residues 66–72 serving as the linker between β2 and β3. Met68 and adjacent residues that are part of the linker will therefore exist in variable structural environments, consistent with the heterogeneity observed for Met68 resonances in solid-state NMR spectra of human αB (17). Heteronuclear NOEs measured in solution on a truncated ACD dimer indicated flexibility for these residues (17) and the β2 strand is present in only one subunit of a dimer in an X-ray structure of a truncated ACD dimer (11). In published crystallographic studies of αB ACDs, protein constructs had to be truncated at Met68 to obtain crystals (11, 12). Variability in β2 is also a feature in other sHSP structures: The ACD from *Methanococcus janashii* sHSP16.5 has a β2 and a β1 strand (20), sHSP16.9 from wheat lacks a β1 strand (23), and Tsp36 from tapeworm has shorter β2 strands compared to sHSP16.5 and sHSP16.9 (24). In summary, this segment appears to adopt multiple structures in multiple environments, thereby contributing to αB's inherent heterogeneity.

The 24-mer model positions two $\beta 1/\beta 2$ loops in close proximity (Fig. 3*B*). To test the model's validity, single cysteine residues were substituted at positions within the β1-loop-β2 sequence to ascertain whether disulfides can form within oligomeric αB samples (αB contains no Cys residues in its sequence). Cross-links are formed within multimers comprised of αB mutants with Cys substitution at A57, S59, or T63, but not at a position within the ACD, V145 (Fig. S4). This finding corroborates the proximity of two β1/β2 loops within an αB multimer connecting two dimers with each other, comparable to the esterase structure used to model these loops.

Positioning of the β1/β2 loops as described above left unoccupied density in the EM map into which residues 1–44 were fitted. The density is observed when looking onto the threefold axis defined by a hexamer, but viewed from the far side (Fig. 3*A*, *Center*). The density is low, suggesting occupancy by loosely packed and/or flexible residues. N-terminal deletion constructs of the closely related αA-crystallin that lack the first 35 residues form multimers of a size comparable to the full-length protein (25). Together with the observation that αB constructs lacking the entire N-terminal domain do not form large multimers (21, 22), we assign residues in the second half of the N-terminal domain of αB as important for the formation of multimers. Two fragments, each consisting of α1 and α2 (see Fig. 2), were docked to each other assigning hydrophobic residues in the more C-terminal helix (Leu32, Leu33, Leu37, and Phe38) as interacting residues in HADDOCK. Three copies of the resulting structure, each comprised of two copies of residues 10–39 with intermolecular interactions involving residues in α2, were modeled into the empty density on the threefold axis in the 24-mer (Fig. 3*C*). The arrangement places the hydrophilic segment Thr40-Ser41-Thr42-Ser43 on the surface of the 24-mer, with α2 residing in the shell of the EM map. Residues 1–44 are likely to be dynamic due to exchange of subunits among the ensemble of multimers, and the model should be viewed as a transient rather than static model.

Finally, flexible residues of the N and C termini identified by NMR were included in the model (Fig. 3 *D* and *E*). Because of different orientations of the ACDs, and therefore the IXI motifs bound to them, half the subunits in a 24-mer have their C-terminal residues 166–175 on the surface and half have them pointing to the interior (Fig. 3*D*). Residues 1–10, including parts of putative α1, were loosely packed in the interior to produce a model that fits radius of gyration measurements by SAXS (see below). Fig. 3*E* and Fig. S5*C* show stereoviews of an αB 24-mer comprised of full-length subunits. A central hollow with an approximately 4-nm diameter is surrounded by flexible residues from the N and C termini.

Heterogeneity of αB. SAXS data measured at pH 7.5 were used to assess the 24-mer model. The experimental curve was compared to the curve calculated for the 24-mer (Fig. 4*A*). The calculated

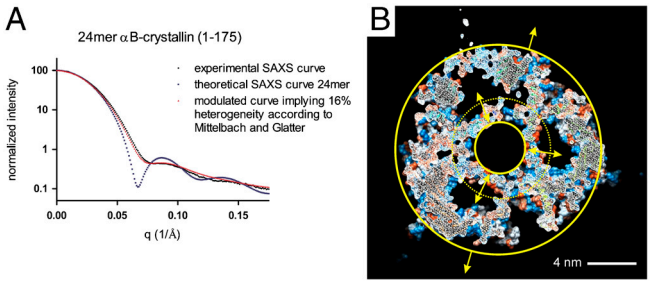

Fig. 4. SAXS analysis of αB reveals heterogeneity. (*A*) SAXS data (black) were compared with the theoretical SAXS curve (blue) calculated for the 24-mer shown in Fig. 3*D*. A theoretical SAXS curve assuming 16% heterogeneity (28) is shown (red). (*B*) Cutaway view of the inner hollow occupied by flexible N-terminal residues and half the flexible C termini. The inner solid circle defines the inner cavity and the dashed circle defines the region occupied by flexible residues, placed to be in agreement with the radius of gyration measured by SAXS.

SAXS curve is typical for a hollow particle, consistent with the model that has an inner hollow diameter of 4 nm and a 4-nm-wide ring occupied by flexible and/or disordered N and C termini (Fig. 4*B*). The radius of gyration measured by SAXS is consistent with the model. The hollow feature observed in two previous EM studies (13, 26) is not recapitulated in the experimental SAXS curve. However, Haley et al. later postulated variable density in the center of the αB oligomer (27).

The SAXS curve calculated for the 24-mer model fits the experimental curve with a χ^2 of 10.8. Heterogeneity of a particle's diameter and shape can modulate the observed SAXS profile of an ensemble of particles. To generate a better fit to the data, we used an algorithm that allows determination of heterogeneity of an ensemble of colloidal particles whose radii vary from SAXS curves. The algorithm essentially modulates the SAXS curve predicted for a homogeneous species by assuming a Schulz distribution for the particles' radii (28). Introduction of a "degree of polydispersity" of 16% produced a fit to the experimental αB SAXS curve with a χ^2 of 1.0. In the case of αB, this heterogeneity parameter cannot be interpreted directly as a distribution of the particles' radii per se, because both size and shape polydispersity are likely to be present simultaneously. Notably, shape polydispersity has been shown to result in overestimation of size polydispersity (29). Nevertheless, we have included the estimated Schulz distribution of the outer particle's radius in Fig. S5*D*. The Schulz distribution of the radius (5.5—9.5 nm) is in good agreement with the radius determined by cryo-EM (5.5—8 nm; 26) taking the 3.6-nm resolution of the cryo-EM data into account. The inferred variable radii of αB multimers could result from an expansion due to incorporation of additional subunits and/or from dynamic C- and N-terminal extensions in the interior of the oligomer. The N- and C-terminal residues can undergo dynamic fluctuations to produce a variable shell thickness within multimers, resulting in a "breathing" of the spherical particle (represented in Fig. 4*B* between the inner and dashed circles). Internal flexibility of dimers within a multimer and the exchange of subunits can also alter the apparent size of the particle, with the SAXS data producing a static "average" image of a heterogeneous population. A cavity with *ca.* 8-nm diameter was determined from EM-density maps calculated using single particle reconstruction (13, 26). In this process, particles are averaged to reconstruct a structure, so density from flexible or disordered regions is averaged out, producing an apparently larger cavity.

Modeling Higher-Order Multimers of αB. It is well established that αB exists as a heterogeneous population of multimers with a variable number of subunits (14). A 24-mer is the simplest species to model due to its symmetry characteristics, but it represents only about 5% of multimeric species as detected by mass spectrometry (14). Therefore, a realistic view of αB assemblies must include higher-order multimers. Given our earlier results showing a dimer to be the basic building block, formation of higher-order multimers likely occurs via incorporation of dimers into existing openings in the shell of the 24-mer. The EM density contains six gaps with dimensions that can accommodate a dimer at the edges of the three twofold axes. Thus, a 26-mer would contain one additional dimer in any one of these openings; a 28-mer would contain two dimers, distributed randomly (Fig. 5*A*), and so forth. Figs. 5 *B* and *C* show a 28-mer with two dimers (green and yellow chains) residing in the edge openings of one twofold axis (indicated with a dotted line and arrows at the edges), viewed onto that twofold axis. Viewed along this twofold axis, the same 28-mer is seen to have its additional dimers in the central openings, one at the front and one at the back of this view (Fig. 5 *D* and *E*). We previously reported intersubunit contacts between β2 residues Ser59-Phe61 and a β3 strand in the ACD, observed by NMR (10). This intersubunit β2 contact is not satisfied in the 24-mer model and must therefore exist in other species. Accordingly, two $\beta 2_{\text{free}}$ strands from two dimer units in a 24-mer crossing

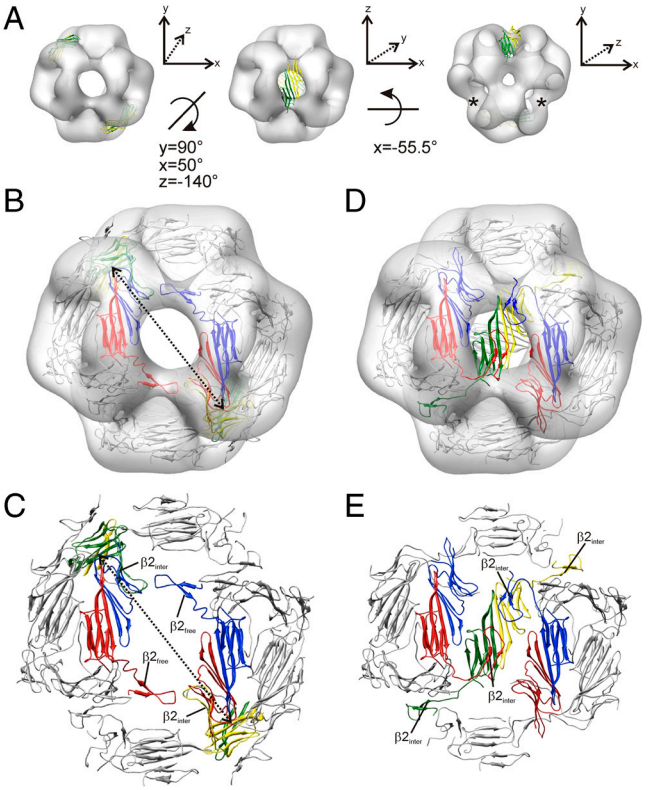

Fig. 5. Model of an αB 28-mer. The EM density of αB has six openings on the edges of the three twofold axes. Each opening is large enough to accommodate an additional dimer. (*A*) Three views of EM density (EMD-1776) showing two additional dimers (each colored green and yellow) in openings at the edges of a twofold axis. (*Left*) View onto a twofold axis with its edge openings filled; (*Center*) view along a different twofold axis, showing the two dimers as placed in the left view; (*Right*) view along a threefold axis, again showing the two dimers as placed in the left-hand panel. Cartesian axes and the axis of rotation are shown for the three perspectives; the same views are shown in *B*–*E*. Asterisks (*Right*) indicate openings without an integrated dimer. (*B*) View as in *A*, *Left*, showing a 24-mer model (red, blue, and gray) and two additional dimers. (*C*) Cropped view of *B* with EM density removed to illustrate the arrangement of β-strands around the opening of the shell in one of the twofold axes. The two additional dimers of the 28-mer are covered in *B* and *C* by the other molecules in the multimer. (*D*) The same oligomer as in *B* is viewed as in *A*, *Center*. The two dimers that break the symmetry of the multimer are shown in green/yellow and gray (on the far side). (*E*) A cropped view of *D* with EM density removed to highlight structural rearrangements of the $\beta 2_{\text{free}}$ to $\beta 2_{\text{inter}}$ strand.

an unoccupied twofold axis become $\beta 2_{inter}$ strands by contacting β3 strands of a new ACD dimer, integrating the new dimeric unit into a larger multimer (Fig. S3*B*). A dimer integrated in this manner can participate in additional intermolecular interactions with its N-terminal and C-terminal domain (Fig. 5*E*). This mode of multimerization allows the formation of multimers of up to 36 subunits, with 24-mers serving as a conserved scaffold into which six additional dimers can be randomly distributed. Given the dynamic behavior of the regions involved in forming higher-order multimers, it is likely that αB multimers undergo exchange so that dimers and/or monomers that comprise the 24-mer scaffold can be replaced by dimers in a twofold axis and vice versa.

Electron Microscopy and Single Particle Analysis of Negatively Stained αB. At the surface, the heterogeneity of αB observed in our solid-state NMR and SAXS data appears at odds with recent 3D reconstructions derived from negative-stain EM studies (13). We therefore analyzed our heterogeneous preparation of αB by negative-stain electron microscopy. In a representative image of the preparation, particles appear homogeneous in size and are evenly dispersed on the grid (Fig. 6*A*). Projection averages were calculated from 4,398 particles (30). Six highly populated class averages are presented as insets. The particles measure approximately 13.6 nm in diameter, with some averages displaying a cavity approximately 4 nm in diameter. These projection averages are comparable to recently published data (Fig. 6*B*) (13). Back projections calculated from the published map of αB (EMD-1776) (13) appear comparable to class averages calculated from our data (compare Fig. 6*A*, *Inset* with 6*C*). Back projections were also calculated for our models of αB multimers containing 24, 26, and 28 subunits (Fig. 6*C* and Fig. S6 *A*–*C*). The calculated projections are similar to each other and to those calculated from the published EM density. Our analysis indicates that single particle reconstructions of negatively stained preparations cannot unambiguously distinguish among several species that are likely to coexist in a heterogeneous population of αB. Thus, although the heterogeneity observed in solid-state NMR data and SAXS data of αB appear to be in conflict with the EM studies [both ours and previously published (13)], it is clear that the size deviations of αB multimers calculated from SAXS data (Fig. 4 and Fig. S5*D*) fall below the approximately 20 Å-resolution limit of negative staining.

Discussion

The model based on NMR observations reveals four regions of αB that are involved in its multimerization. First, two β6+7 strands within the ACD align to form a homodimer, the smallest building block (Fig. S1*A*) (10). Second, the conserved IXI motif from the C terminus of one dimer binds to hydrophobic pockets formed by the β4 and β8 strands on the edge of another dimer (Fig. S1*B*). This interaction creates a triangular array of three dimers that defines the threefold axis (Fig. S1*C*). Third, the β2 strand is involved in variable interactions: β2 can contact β3 intramolecularly or intermolecularly (Figs. 3 and 5). Fourth, N-terminal residues interact at the edge of the threefold axis. Thus, the ACD is responsible for dimer formation, the ACD dimer and the C-terminal regions are responsible for defining hexameric units, and the N-terminal region and ACD are responsible for higher-order multimerization. The regions involved in multimerization in the model are in good agreement with sequences identified by peptide-binding assays as involved in αB self-assembly: Leu37-Pro58, Phe75-Lys82 (β3), Leu131-Ser139 (β8), Gly141-Pro148 (β9), and Pro158-Glu165 (containing the IXI motif) (31).

The ACD dimer has a twisted conformation, which results in two orientations of the six subunits within a hexameric unit. The β4/β8 substrate-binding groove at the edge of each ACD, occluded by the C-terminal IXI motif, faces toward the outside in half the subunits and to the inside of a multimer in the other half (Fig. S5 *A* and *B*). Dissociation of an IXI motif from the groove in response to activation of αB by pH (10) would presumably occur primarily in the outward-facing copies, leaving half the interactions in place to retain the hexameric unit. Virtually all residues of the protein are solvent accessible somewhere in the multimer, with the exception of the extreme N terminus and helices α1 and α2, which are packed in the density at the edge of a threefold axis or tucked on the inside. In this context, it is notable that the N-terminal domain itself forms disordered aggregates (22, 25), so sequestration of this region in multimers may be important to prevent stochastic oligomerization. The observation that all other regions of αB are accessible in a multimer may explain why almost all regions have been implicated in the binding of one or more client proteins (31, 32). Of note, the high abundance of known phosphorylation sites (33) at one edge of the threefold axis suggests the presence of a binding interface for kinases in this region (Fig. S7).

The model provides structural context for known mutations in αB associated with its dysfunction and/or disease. The best characterized of these is R120G-αB (34); Arg120 interacts with Asp109 from the other subunit across the ACD dimer interface so its substitution may affect αB structure at the level of the dimer.

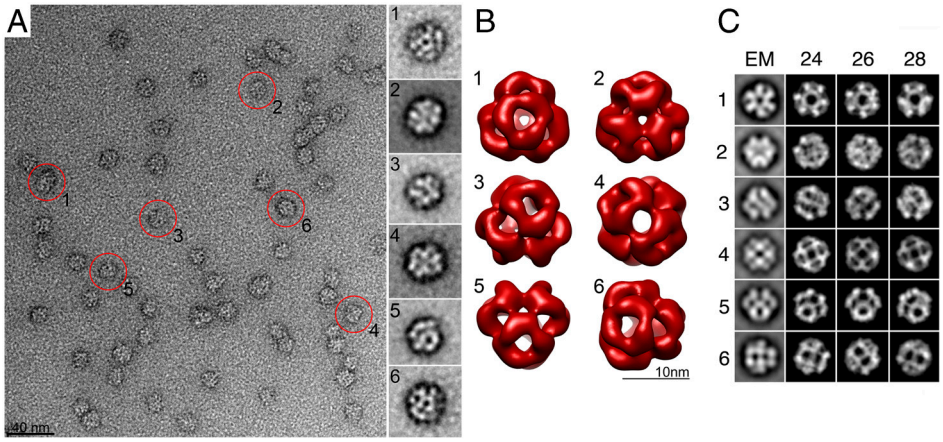

Fig. 6. Electron microscopy and single particle analysis of αB. (*A*) Representative micrograph of negatively stained αB. The particles appear homogeneous in size. (*Inset*) Examples of six prominent class averages calculated using reference-free multivariant statistical analysis procedures in SPIDER (30). Red circles identify examples of the six class averages. The width of the box of the projection averages is 27 nm. (*B*) Different views of the αB density map (EMD-1776) at 20-Å resolution (13). The six views presented correspond to the six class averages shown in *A*, *Inset*. (*C*) Calculated back projection of the density map presented in *B*, and from models of αB 24-, 26-, and 28-mers. The six chosen back projections correspond to the six class averages in *A* and to the views in *B*.

The D140N mutation (35) could affect a putative intermolecular salt bridge with Arg56 in the N-terminal region, thereby affecting higher-order structure (36). The early truncation mutant Q151X (37) lacks the IXI motif, which plays a role in the formation of hexamers and the extreme C terminus that is responsible for the high solubility of αB oligomers. Furthermore, variable intra- and intermolecular interactions of β-strands, a hallmark of amyloid-forming proteins (38, 39), provide an explanation for the propensity of fibril formation of αB (16).

In conclusion, αB is a highly dynamic assembly with flexible termini that contribute substantially to its heterogeneous appearance. The model we present here suggests a simple mechanism by which αB dimeric units serve as building blocks that can add to a symmetric 24-mer assembly to form higher-order multimers with minimal conformational change. This model for assembly therefore also allows for facile exchange of subunits with minimal energy. The interactions that define higher-order multimers are all the same and are essentially the same as those that define the 24-mer, consistent with the broad distribution of species observed and indicative of equivalent stabilities. Although the resulting ensemble of multimers cannot be distinguished at the level of EM analysis on negatively stained preparations, the presence of multimers with varying symmetries presumably contributes to the prevention of crystal- and high-molecular weight aggregate formation, an essential property for biological functions of αB, which occurs in high concentrations in the eye lens.

Materials and Methods

Details are provided in *SI Text*.

αB was expressed, purified, and solid-state NMR spectra were recorded as described elsewhere (10, 17). SAXS data were collected at the European Molecular Biology Laboratory SAXS X33 beamline, Hamburg, Germany.

For electron microscopy, a 2-μL drop of αB at pH 7.5 in 50 mM sodium phosphate, 100 mM NaCl was applied to freshly glow-discharged electron microscopy grid and stained with 2% uranyl acetate. The preparation was viewed on a 100-kV transmission electron microscope (Morgagni M268, FEI) and images recorded at a nominal magnification of 67,000× at the specimen level using a bottom-mount 4 k × 2 k Gatan CCD camera, corresponding to a pixel size of 1.34 Å.

ACKNOWLEDGMENTS. We thank J. Buchner, S. Weinkauf, and N. Braun for providing their EM map prior to deposition. This work was funded by National Institutes of Health (NIH) Grant 1R01 EY017370 (to R.E.K.). B.V. is supported in part by NIH 2T32 GM007270. T.G. is supported by NIH Grant 1R01 GM079233, American Diabetes Association (Award 1-09-CD-05) and by Howard Hughes Medical Institute Early Career Scientist Award.

1. Bukau B, Weissman J, Horwich A (2006) Molecular chaperones and protein quality control. *Cell* 125:443–451.
2. Haslbeck M, Franzmann T, Weinfurtner D, Buchner J (2005) Some like it hot: The structure and function of small heat-shock proteins. *Nat Struct Mol Biol* 12:842–846.
3. Ecroyd H, Carver JA (2009) Crystallin proteins and amyloid fibrils. *Cell Mol Life Sci* 66:62–81.
4. Horwitz J (1992) Alpha-crystallin can function as a molecular chaperone. *Proc Natl Acad Sci USA* 89:10449–10453.
5. Vicart P, et al. (1998) A missense mutation in the alphaB-crystallin chaperone gene causes a desmin-related myopathy. *Nat Genet* 20:92–95.
6. Goldstein LE, et al. (2003) Cytosolic beta-amyloid deposition and supranuclear cataracts in lenses from people with Alzheimer's disease. *Lancet* 361:1258–1265.
7. Kato K, et al. (2001) Ser-59 is the major phosphorylation site in alphaB-crystallin accumulated in the brains of patients with Alexander's disease. *J Neurochem* 76:730–736.
8. Ousman SS, et al. (2007) Protective and therapeutic role for alphaB-crystallin in autoimmune demyelination. *Nature* 448:474–479.
9. Augusteyn RC, Koretz JF (1987) A possible structure for alpha-crystallin. *FEBS Lett* 222:1–5.
10. Jehle S, et al. (2010) Solid-state NMR and SAXS studies provide a structural basis for the activation of alphaB-crystallin oligomers. *Nat Struct Mol Biol* 17:1037–1042.
11. Bagneris C, et al. (2009) Crystal structures of alpha-crystallin domain dimers of alphaB-crystallin and Hsp20. *J Mol Biol* 392:1242–1252.
12. Laganowsky A, et al. (2010) Crystal structures of truncated alphaA and alphaB crystallins reveal structural mechanisms of polydispersity important for eye lens function. *Protein Sci* 19:1031–1043.
13. Peschek J, et al. (2009) The eye lens chaperone alpha-crystallin forms defined globular assemblies. *Proc Natl Acad Sci USA* 106:13272–13277.
14. Aquilina JA, Benesch JL, Bateman OA, Slingsby C, Robinson CV (2003) Polydispersity of a mammalian chaperone: Mass spectrometry reveals the population of oligomers in alphaB-crystallin. *Proc Natl Acad Sci USA* 100:10611–10616.
15. Carver JA, Aquilina JA, Truscott RJ, Ralston GB (1992) Identification by 1H NMR spectroscopy of flexible C-terminal extensions in bovine lens alpha-crystallin. *FEBS Lett* 311:143–149.
16. Meehan S, et al. (2007) Characterisation of amyloid fibril formation by small heat-shock chaperone proteins human alphaA-, alphaB- and R120G alphaB-crystallins. *J Mol Biol* 372:470–484.
17. Jehle S, et al. (2009) alphaB-crystallin: A hybrid solid-state/solution-state NMR investigation reveals structural aspects of the heterogeneous oligomer. *J Mol Biol* 385:1481–1497.
18. Higman VA, et al. (2009) Assigning large proteins in the solid state: A MAS NMR resonance assignment strategy using selectively and extensively ^{13}C-labeled proteins. *J Biomol NMR* 44:245–260.
19. Shen Y, Delaglio F, Cornilescu G, Bax A (2009) TALOS+: A hybrid method for predicting protein backbone torsion angles from NMR chemical shifts. *J Biomol NMR* 44:213–223.
20. Kim KK, Kim R, Kim SH (1998) Crystal structure of a small heat-shock protein. *Nature* 394:595–599.
21. Kundu B, Shukla A, Chaba R, Guptasarma P (2004) The excised heat-shock domain of alphaB crystallin is a folded, proteolytically susceptible trimer with significant surface hydrophobicity and a tendency to self-aggregate upon heating. *Protein Expres Purif* 36:263–271.
22. Merck KB, De Haard-Hoekman WA, Oude Essink BB, Bloemendal H, De Jong WW (1992) Expression and aggregation of recombinant alpha A-crystallin and its two domains. *Biochim Biophys Acta* 1130:267–276.
23. van Montfort RL, Basha E, Friedrich KL, Slingsby C, Vierling E (2001) Crystal structure and assembly of a eukaryotic small heat shock protein. *Nat Struct Biol* 8:1025–1030.
24. Stamler R, Kappe G, Boelens W, Slingsby C (2005) Wrapping the alpha-crystallin domain fold in a chaperone assembly. *J Mol Biol* 353:68–79.
25. Augusteyn RC (1998) alpha-Crystallin polymers and polymerization: The view from down under. *Int J Biol Macromol* 22:253–262.
26. Haley DA, Horwitz J, Stewart PL (1998) The small heat-shock protein, alphaB-crystallin, has a variable quaternary structure. *J Mol Biol* 277:27–35.
27. Haley DA, Bova MP, Huang QL, McHaourab HS, Stewart PL (2000) Small heat-shock protein structures reveal a continuum from symmetric to variable assemblies. *J Mol Biol* 298:261–272.
28. Mittelbach R, Glatter O (1998) Direct structure analysis of small-angle scattering data from polydisperse colloidal particles. *J Appl Crystallogr* 31:600–608.
29. Vass S, et al. (2008) Ambiguity in determining the shape of alkali alkyl sulfate micelles from small-angle scattering data. *Langmuir* 24:408–417.
30. Frank J, et al. (1996) SPIDER and WEB: Processing and visualization of images in 3D electron microscopy and related fields. *J Struct Biol* 116:190–199.
31. Ghosh JG, Clark JI (2005) Insights into the domains required for dimerization and assembly of human alphaB crystallin. *Protein Sci* 14:684–695.
32. Ghosh JG, Shenoy AK, Jr, Clark JI (2006) N- and C-terminal motifs in human alphaB crystallin play an important role in the recognition, selection, and solubilization of substrates. *Biochemistry* 45:13847–13854.
33. MacCoss MJ, et al. (2002) Shotgun identification of protein modifications from protein complexes and lens tissue. *Proc Natl Acad Sci USA* 99:7900–7905.
34. Vicart P, et al. (1998) A missense mutation in the alphaB-crystallin chaperone gene causes a desmin-related myopathy. *Nat Genet* 20:92–95.
35. Liu Y, et al. (2006) A novel alphaB-crystallin mutation associated with autosomal dominant congenital lamellar cataract. *Invest Ophth Vis Sci* 47:1069–1075.
36. Biswas A, et al. (2007) Paradoxical effects of substitution and deletion mutation of Arg56 on the structure and chaperone function of human alphaB-crystallin. *Biochemistry* 46:1117–1127.
37. Selcen D, Engel AG (2003) Myofibrillar myopathy caused by novel dominant negative alpha B-crystallin mutations. *Ann Neurol* 54:804–810.
38. Routledge KE, Tartaglia GG, Platt GW, Vendruscolo M, Radford SE (2009) Competition between intramolecular and intermolecular interactions in an amyloid-forming protein. *J Mol Biol* 389:776–786.
39. Pechmann S, Levy ED, Tartaglia GG, Vendruscolo M (2009) Physicochemical principles that regulate the competition between functional and dysfunctional association of proteins. *Proc Natl Acad Sci USA* 106:10159–10164.